Journal of ELECTRONIC MATERIALS, Vol. 48, No. 4, 2019
https://doi.org/10.1007/s11664-019-06958-5

TOPICAL COLLECTION: INTERNATIONAL CONFERENCE ON THERMOELECTRICS 2018

Effects of Cobalt Substitution on Crystal Structure and Thermoelectric Properties of Melt-Grown Higher Manganese Silicides

H. NAGAI,[1,2] H. HAMADA,[1] K. HAYASHI,[1] and Y. MIYAZAKI[1]

1.—Department of Applied Physics, Graduate School of Engineering, Tohoku University, 6-6-05, Aramaki, Aoba, Sendai, Miyagi 980-8579, Japan. 2.—e-mail: nagai@crystal.apph.tohoku.ac.jp

To improve the thermoelectric (TE) properties of melt-grown higher manganese silicides $MnSi_\gamma$, dissipation of MnSi precipitates that deteriorate the electrical conductivity is required. We have investigated the effects of light cobalt (Co) substitution on TE properties and MnSi precipitates of $MnSi_\gamma$. A 4% substitution of Mn with Co is an effective approach to eliminate MnSi precipitates from melt-grown $MnSi_\gamma$, which is confirmed by powder x-ray diffraction and energy-dispersive spectroscopy measurements. Furthermore, this light Co substitution leads to increase of the hole carrier concentration, resulting in a great increase in the electrical conductivity from 24×10^3 S/m to 54×10^3 S/m at 700 K. The resulting power factor exhibits 1.9×10^{-3} W/mK^2 around 700 K. Moreover, the lattice thermal conductivity is greatly decreased by partial Co substitution compared with that of Co-free $MnSi_\gamma$. Consequently, the dimensionless figure-of-merit zT of $(Mn_{1-x}Co_x)Si_\gamma$ samples increases from 0.27 for $x = 0$ to 0.50 for $x = 0.04$ in the vicinity of 800 K.

Key words: Higher manganese silicides, valence electron counts, thermoelectric properties, MnSi precipitate, cobalt substitution

INTRODUCTION

Higher manganese silicides (HMSs), such as $MnSi_\gamma$, have attracted much interest as good candidates for thermoelectric (TE) materials because of their reasonable chemical stability at high temperature,[1] low toxicity, and the natural abundance of their constituents. This is also true of other silicides, for example, Mg_2Si[2–4] and β-$FeSi_2$.[5–7] Although crystal structures of $MnSi_\gamma$ have been reported as Mn_4Si_7,[8] $Mn_{11}Si_{19}$,[9,10] $Mn_{15}Si_{26}$,[11] and $Mn_{27}Si_{47}$,[12] it was pointed out that these compounds can be described as a single-compound $MnSi_\gamma$ using the (3 + 1)-dimensional super-space group.[13] Based on this description, $MnSi_\gamma$ possesses two tetragonal subsystems of [Mn] and [Si]. These subsystems have the same a-axis length and an irrational c-axis parameter $\gamma = c_{Mn}/c_{Si}$ of ~ 1.74.[13] This γ value also represents the compositional ratio of Mn and Si, which is characteristic of a Nowotny chimney ladder phase. As understood from the characteristic crystal structure of $MnSi_\gamma$, this compound has large anisotropic physical properties. It has been reported that $MnSi_\gamma$ at room temperature exhibits, along the c axis, an electrical conductivity of $\sim 10 \times 10^3$ S/m, a Seebeck coefficient of ~ 200 μV/K, and a thermal conductivity of ~ 2 W/mK.[14] In contrast, at room temperature, $MnSi_\gamma$ exhibits a higher electrical conductivity ($\sim 70 \times 10^3$ S/m), a lower Seebeck coefficient (~ 100 μV/K), and a higher thermal conductivity (~ 3 W/mK) perpendicular to the c axis, i.e., in the ab plane.

The performance of TE materials is generally evaluated by the dimensionless figure-of-merit zT ($= S^2\sigma T/\kappa$, where S is the Seebeck coefficient, σ is the electrical conductivity, T is the absolute temperature, and κ is the thermal conductivity). To

(Received August 21, 2018; accepted January 12, 2019; published online February 12, 2019)

date, many attempts to improve the zT of $MnSi_\gamma$ have been reported.[15–23] For example, Yamamoto et al.[19] succeeded in the preparation of a sample with $zT > 1$ by heavy Re substitution using a melt-spinning method. Miyazaki et al.[20,21] reported a power factor (PF; $= S^2\sigma$) exceeding 2.3×10^{-3} W/mK^2 by preparing slightly V-substituted melt-grown samples. Moreover, Miyazaki et al. discovered how to completely eliminate MnSi precipitates from the melt-grown samples. When $MnSi_\gamma$ is prepared in a liquid phase by means such as the Bridgman method, MnSi precipitates are always linearly formed as a primary crystal and run along the direction perpendicular to the c axis of $MnSi_\gamma$.[24] These precipitates scatter carriers at the boundary, resulting in the deterioration of the electrical conductivity. It has been reported that several kinds of elemental substitution are effective in suppressing MnSi precipitates. By V substitution of Mn sites[20,21] (as mentioned above) and Ge substitution of Si sites,[15,16,21] these linear precipitates become thin or completely dissipate. Miyazaki et al.[21] suggested that a reason for the formation of MnSi precipitates is the difference in the coefficient of thermal expansion between [Mn] and [Si] subsystems, and they predicted that the γ value of ~ 1.72 is suitable for suppression of the precipitates. Indeed, the reported γ values of Ge- and V-substituted samples were approximately 1.73 and 1.725, respectively, which are lower than that of the sample without elemental substitution.[21] Hence, reduction of γ should be an effective approach to eliminate MnSi precipitates.

Another element that decreases the γ value is cobalt (Co), which can substitute at the Mn site.[17] Polycrystalline $(Mn_{1-x}Co_x)Si_\gamma$ (x = 0, 0.05, 0.08, 0.10, 0.15, and 0.20) samples were prepared using arc melting and spark plasma sintering. According to the aforementioned report, the γ value decreased from ~ 1.73 to ~ 1.715 with an increase in Co content up to x = 0.10. This γ value is smaller than those of Ge- or V-substituted samples.[21] Therefore, it is expected that MnSi precipitates in the melt-grown samples are eliminated by Co substitution. Furthermore, the reduction of γ effectively works as hole carrier doping. The electrical transport properties of $MnSi_\gamma$ can be evaluated using the valence electron count (VEC) expressed as VEC = 7 + 4γ, where the 7 and 4 are the number of valence electrons of Mn and Si, respectively. The VEC for pure $MnSi_\gamma$ with γ = 1.74 is 13.96. Because the VEC of $MnSi_\gamma$ is less than 14, $MnSi_\gamma$ exhibits p-type conduction. The decrease in VEC corresponds to the increase in hole carrier concentration. In $(Mn_{1-x}Co_x)Si_\gamma$ solid solution, the VEC can be represented by the formula VEC = $7(1 - x) + 9x + 4\gamma$, where the 9 is the number of valence electrons of Co. Now, rewritten for simpler consideration, the above formula can be represented as VEC = 7 + 2 x + 4γ. Co substitution leads to a decrease in γ. However, the increase in x should also be taken into account for describing the change in VEC. Therefore, it might be difficult to expect that VEC decreases with an increase in Co content. According to Ref. 17, the experimentally obtained VEC of Co-substituted samples increased with an increase in Co content. Their electrical conductivity and Seebeck coefficient increased and decreased, respectively. However, the relationship between VEC and Co content for $x < 0.05$, and their microstructure, has not been reported to date.

In this study, we report on the crystal structure, microstructure, and TE properties of lightly Co-substituted melt-grown $MnSi_\gamma$, $(Mn_{1-x}Co_x)Si_\gamma$ ($x \le 0.08$). In particular, the effects of Co substitution on MnSi precipitates and VEC were investigated.

EXPERIMENTAL

Samples with nominal compositions of $(Mn_{1-x}Co_x)Si_\gamma$ (x = 0–0.08) were prepared. First, we prepared all Co-substituted samples with a Si nominal composition of 1.74. However, the obtained samples possessed a considerable amount of a secondary phase of $CoSi_2$. Hence, to reduce the amount of secondary phase, their Si nominal compositions were adjusted using a refined γ value (refined by Rietveld analysis, which will be described later). Granular Mn (99.99%), Co (99.9%), and Si (99.999%) were melted in an arc-melting furnace (G.E.S., GMAC-1100). The obtained ingots were crushed into small pieces and remelted in evacuated quartz tubes at 1473 K for 8 h. The tubes were then slowly cooled to 1373 K for 100 h to obtain samples possessing large grains like a single crystal.

The phases of the samples after the melt-grown process were identified by powder x-ray diffraction (XRD; Bruker, D8 ADVANCE) using CuK_α radiation at room temperature. The lattice parameters of the samples were refined based on the (3 + 1)-dimensional superspace group by Rietveld analysis using the Jana2006 software package.[25] The backscattering electron images and elemental distribution maps were observed by scanning electron microscopy (SEM; JEOL, JSM-IT100) with energy-dispersive spectroscopy (EDS). From the EDS analysis, it was confirmed that the compositional ratio of Mn and Co for each melt-grown sample was slightly smaller than their nominal composition. However, because the difference is less than 1%, the nominal composition is hereafter used when we refer to samples.

The electrical conductivity and the Seebeck coefficient were measured by a commercial thermoelectric tester (ADVANCE RIKO, ZEM-3) in He atmosphere over the range of room temperature to 1000 K. The thermal conductivity was measured by a laser flash thermal constants analyzer (ADVANCE RIKO, TC-7000) in vacuum. The carrier concentration was evaluated using a physical properties measurement system (PPMS; Quantum

Design) at room temperature. Several cracks were observed in slightly Co-substituted samples ($0 < x < 0.04$). Hence, we measured the TE properties for the $x = 0$ and 0.04 samples, and their relative densities were above 92%. The crystallographic orientation of the samples for evaluating the TE properties was determined by Laue diffraction and was evaluated by field-emission SEM with electron backscattering diffraction (FE-SEM/EBSD; JEOL, JSM-7100F). All TE properties were measured along the $c_\perp$ direction (perpendicular to the c axis).

RESULTS AND DISCUSSION

Figure 1a shows powder XRD patterns of the studied $(Mn_{1-x}Co_x)Si_\gamma$ samples after the melt-grown process. Although Nowotny chimney ladder phases were obtained as a main phase, several kinds of secondary phases were observed in the samples. In the range of $0 \le x \le 0.02$, a MnSi phase was detected at $2\theta \sim 44.4°$. This MnSi phase was not observed in the range of $x > 0.02$, but small amounts of Si and $CoSi_2$ phases were detected around $2\theta \sim 29°$. In addition, as shown in Fig. 1b, a split in the 1101 peak derived from the [Si] subsystem was observed, and the 1101 peak shifted to the lower angle side with an increase in Co content x. This has also been reported for V-substituted samples.[20,21]

Figure 2a–d shows the Co content x dependence of the a-axis and c-axis lengths for Mn- and Si-subsystems and c-axis parameter $\gamma = c_{Mn}/c_{Si}$ of $(Mn_{1-x}Co_x)Si_\gamma$ samples refined by Rietveld analysis. The a- and c_{Mn}-axis lengths of Co-free $MnSi_\gamma$ were $a = 5.5282(1)$ Å and $c_{Mn} = 4.3666(1)$ Å, respectively, which are in good agreement with previous literature values.[20,21] Both the a- and c_{Mn}-axis lengths decreased with an increase in Co content x up to $x \sim 0.04$, which suggests that Mn was partially substituted by Co because the atomic radius of Co, $r_{Co} = 1.35$ Å,[26] is smaller than that of Mn, $r_{Mn} = 1.40$ Å.[26] From this result, it can be concluded that the solubility limit of Co into $MnSi_\gamma$ is ~ 0.04. However, this solubility limit is not in agreement with that of polycrystalline $(Mn_{1-x}Co_x)Si_\gamma$ samples prepared by spark plasma sintering (solubility limit $\sim 10\%$[17]), even though our samples have similar lattice parameters to the report; e.g., a-axis lengths of 5.5154(1) Å at $x = 0.04$ (this work) and ~ 5.515 Å at $x = 0.10$ (from Ref. 17). The difference in the solubility limit between the melt-grown samples and sintered samples resulted from the difference in preparation methods and the adjustment of the Si nominal composition, as shown in Fig. 2d, for the reduction in the secondary phase of $CoSi_2$. The a- and c_{Mn}-lengths of Co-substituted samples with the constant nominal composition of Si ($\gamma = 1.74$) gradually decreased by increasing x up to $x \sim 0.10$, which is similar behavior to that reported previously.[17]

The a- and c-axis lengths exhibited characteristic behavior, which is to say that they did not obey Vegard's law. By increasing x up to $x = 0.01$, the a-axis length slightly decreased, and then it drastically decreased at $x = 0.02$ before gradually decreasing over the range $0.02 < x < 0.04$. However, c_{Si} slightly increased with an increase in x up to $x = 0.01$, and then it drastically increased at $x = 0.02$ before it gradually increased over the range $0.02 < x < 0.04$. These unusual changes in lattice parameters come from the split of the 1101 peak shown in Fig. 1b. Consequently, the c-axis parameter $\gamma = c_{Mn}/c_{Si}$ significantly decreased at $x = 0.02$ because of the split of the 1101 peak. γ gradually decreased to 1.7171(1), which is close to the value reported in Ref. 17 ($\gamma \sim 1.715$ at $x = 0.10$).

As shown in Fig. 2e, the calculated VEC of $(Mn_{1-x}Co_x)Si_\gamma$ increased from 13.968 to 13.978 with x up to $x = 0.01$, and then it dropped to 13.927 at $x = 0.02$ because of the significant decrease in γ.

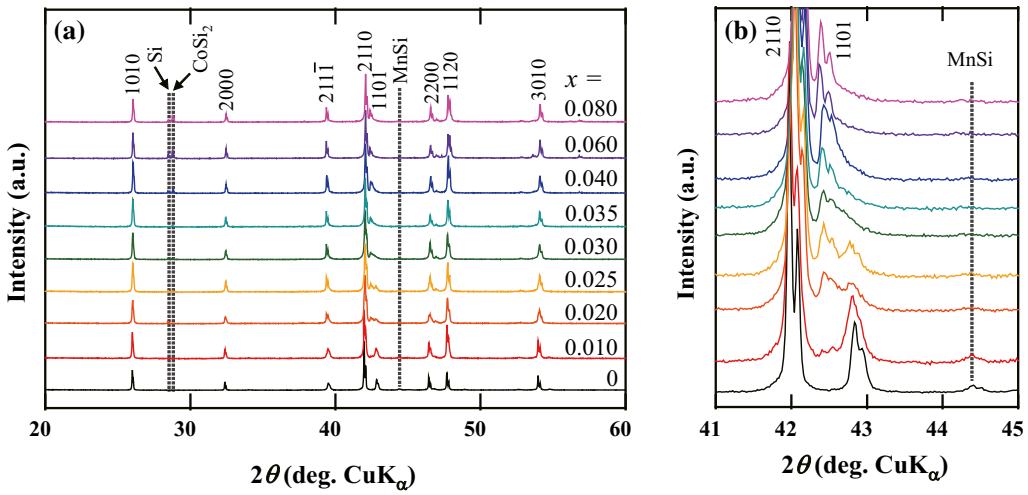

Fig. 1. XRD patterns of $(Mn_{1-x}Co_x)Si_\gamma$ with a 2θ range of (a) 20°–60° and (b) 41°–45°.

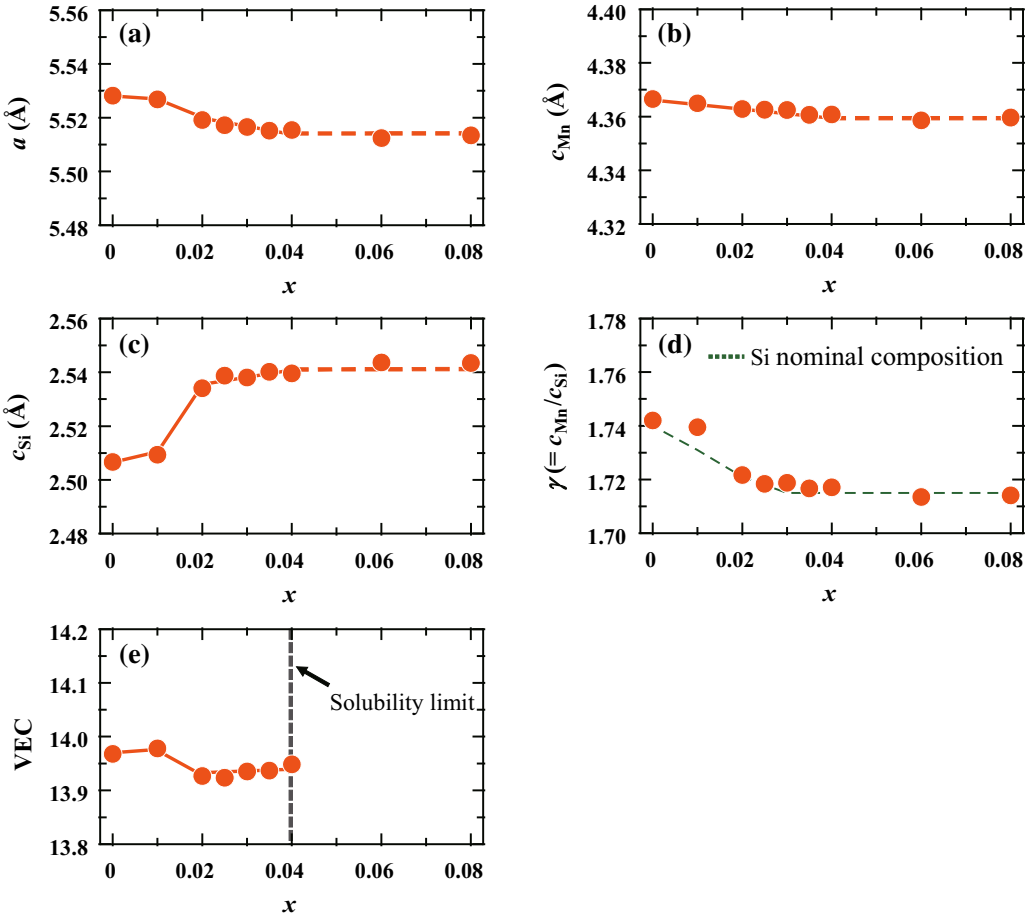

Fig. 2. Co content x dependence of (a) a, (b) c_{Mn}, (c) c_{Si}, (d) γ, and (e) VEC for $(Mn_{1-x}Co_x)Si_\gamma$. The Si nominal composition determined based on the refinement is shown in (d) as a green dashed line (Color figure online).

Finally, the VEC gradually increased up to 13.948 for $x = 0.04$, which is lower than that for $x = 0$. Hence, Co substitution increases the hole carrier concentration in the range of $0.02 \le x \le 0.04$, but not the electron carrier concentration. According to the results of Hall measurements, the carrier concentration at room temperature increased from $8.3(4) \times 10^{20}$ cm^{-3} for the $x = 0$ sample to $3.2(3) \times 10^{21}$ cm^{-3} for the $x = 0.04$ sample. We can conclude that Co substitution of Mn sites in $MnSi_\gamma$ works as hole carrier doping, although valence electrons of Co are larger than those of Mn. Moreover, we have to consider not only the valence of the elements but also the change in the γ value to optimize the carrier concentration by elemental substitution in $MnSi_\gamma$.

Figure 3a–i shows SEM images and EDS maps of the studied $(Mn_{1-x}Co_x)Si_\gamma$ samples. In the $x = 0$ sample, white lines were observed which can be identified as MnSi precipitates based on the EDS maps (see Fig. 3b and c). The number of these lines increased with an increase in Co content x, whereas the thickness of the lines decreased. Similar behavior has been reported in the case of V[20,21] or Ge[15,16,21] substitution. In addition, the increase in the number of precipitates increases the number of the interfaces between precipitates and matrix. Hence, because of the difference in the coefficient of thermal expansion between them, several cracks were observed in the samples with x between 0 and 0.04 as mentioned in the experimental section. Finally, these precipitates completely disappeared when $x > 0.02$, which is consistent with the XRD results.

Figure 4a–c shows the temperature dependence of the electrical conductivity, Seebeck coefficient, and PF of Co-free and Co-substituted samples. The room-temperature electrical conductivity and Seebeck coefficient along $c_\perp$ of the Co-free sample were 67×10^3 S/m and 120 μV/K, respectively, which correspond to those of Ref. 14. By Co substitution, the electrical conductivity and Seebeck coefficient over the temperature range increased and decreased, respectively, reflecting the increase in the hole carrier concentration as mentioned above. Compared with a V-substituted sample,[21] the Co-substituted sample exhibited low electrical conductivity and a higher Seebeck coefficient. This is because the Co-substituted sample possesses a larger VEC, i.e., lower hole carrier concentration,

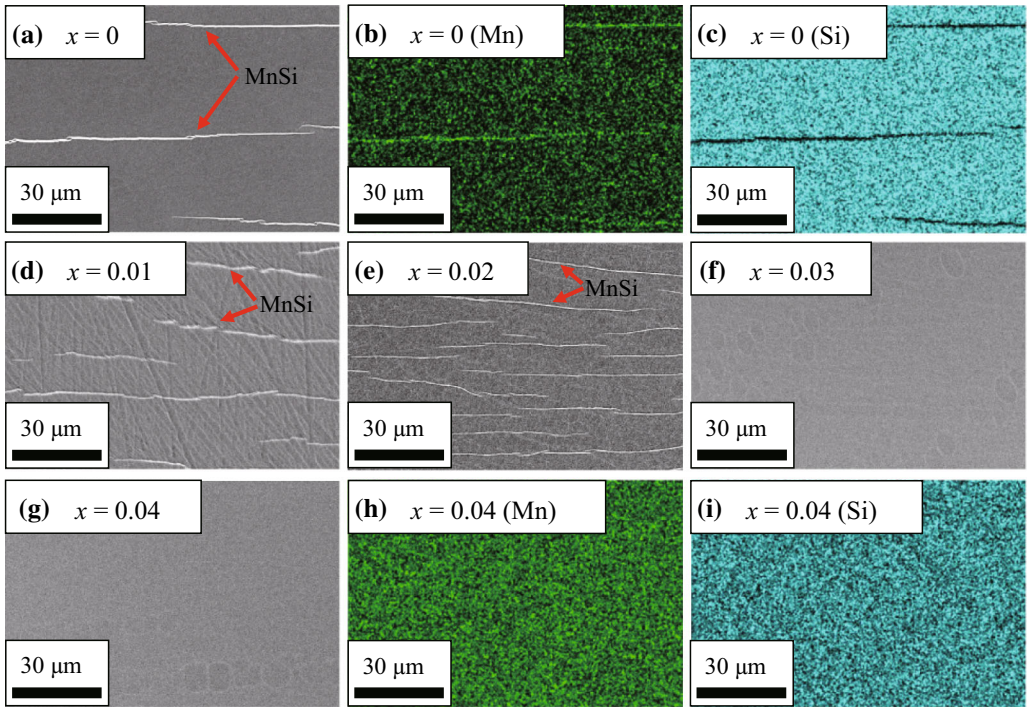

Fig. 3. (a, d–g) SEM images of $(Mn_{1-x}Co_x)Si_\gamma$. EDS maps for (b, h) Mn and (c, i) Si of $x = 0$ and $x = 0.04$ samples, respectively.

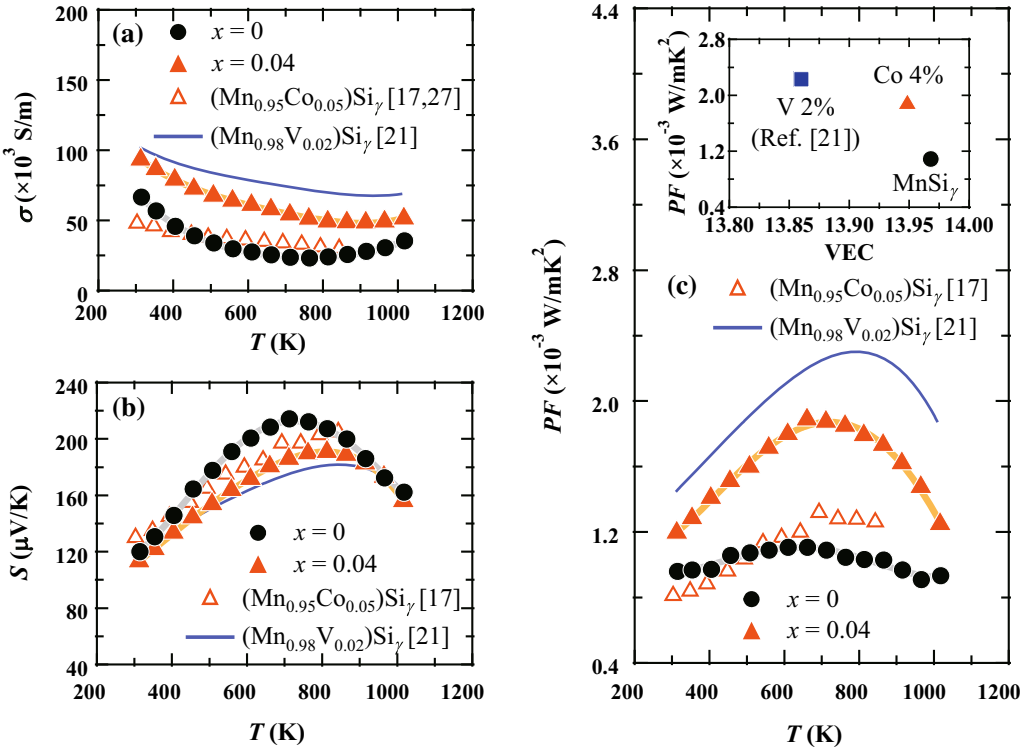

Fig. 4. Temperature dependence of (a) electrical conductivity, (b) Seebeck coefficient, and (c) power factor (PF) along $c_\perp$ for $(Mn_{1-x}Co_x)Si_\gamma$. The inset in (c) shows the relationship between PF at 700 K and VEC.

compared with the V-substituted sample. Consequently, as shown in Fig. 4c, the Co-substituted sample exhibited a significantly higher PF (1.9×10^{-3} W/mK^2) compared with that of the Co-free sample. Moreover, compared with a polycrystalline sample,[17,27] the Co-substituted melt-grown sample exhibited a higher PF due to the high electrical conductivity. However, this PF is still low

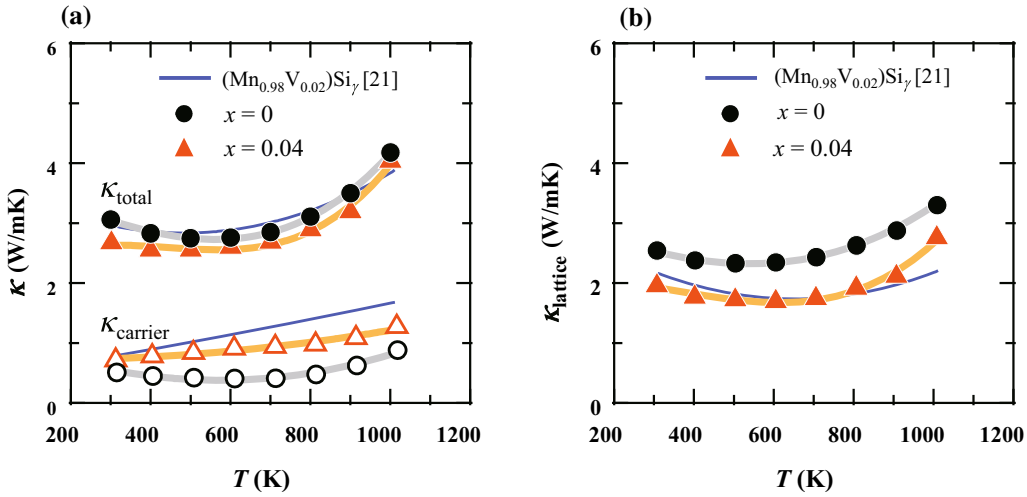

Fig. 5. Temperature dependence of (a) total thermal conductivity (filled circles) and carrier thermal conductivity (open circles), and (b) lattice thermal conductivity along $c_\perp$ for $(Mn_{1-x}Co_x)Si_\gamma$.

compared with that of the V-substituted sample (2.3×10^{-3} W/mK^2[21]) because of the larger VEC, as shown in the inset of Fig. 4c. This result shows that the PF of Co-substituted samples has room for improvement if the VEC is further decreased by double substitution.

Figure 5a shows the temperature dependence of the total thermal conductivity (filled circles) of $(Mn_{1-x}Co_x)Si_\gamma$ samples along $c_\perp$. The total thermal conductivity of the Co-free sample at room temperature was 3.1 W/mK, which is in good agreement with the previous report.[14] The carrier contribution, $\kappa_{carrier}$, is also shown in Fig. 5a as open circles, which is calculated based on the Wiedemann–Franz law: $\kappa_{carrier} = L\sigma T$, where L is the Lorenz number (2.44×10^{-8} WΩ/K^2) for a degenerate semiconductor. The calculated $\kappa_{carrier}$ for the Co-free sample was 0.51 W/mK at room temperature, and it was increased over the temperature range by Co substitution due to the increase in electrical conductivity. The Co-substituted sample exhibited a lower $\kappa_{carrier}$ compared with the V-substituted sample with high electrical conductivity. The $\kappa_{total} - \kappa_{carrier}$ is described as the lattice thermal conductivity $\kappa_{lattice}$ in Fig. 5b. The $\kappa_{lattice}$ greatly decreased at room temperature from 2.5 W/mK ($x = 0$) to 2.0 W/mK ($x = 0.04$). Consequently, κ_{total} of the Co-substituted sample slightly decreased compared with that of the Co-free sample over the temperature range because the $\kappa_{lattice}$ was greatly decreased by partial Co substitution. Moreover, it is found that Co substitution is more effective in reducing κ_{total} compared with V substitution because the Co-substituted sample exhibits a lower $\kappa_{carrier}$ value than the V-substituted sample, although the two samples possess comparable $\kappa_{lattice}$ values.

Figure 6 shows the temperature dependence of zT of $(Mn_{1-x}Co_x)Si_\gamma$ samples along $c_\perp$. The zT value of the Co-free sample increased with an increase in

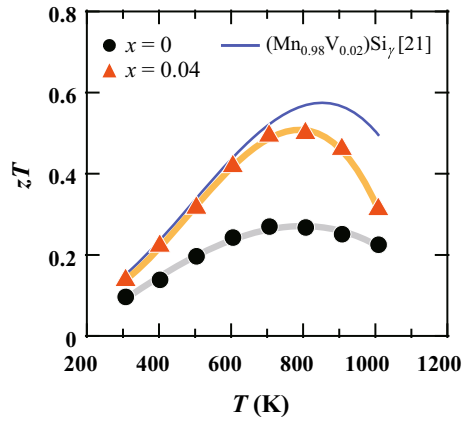

Fig. 6. Temperature dependence of dimensionless figure-of-merit zT along $c_\perp$ for $(Mn_{1-x}Co_x)Si_\gamma$.

temperature and exhibited the maximum, zT_{max}, around 700 K with $zT = 0.27$. Although the zT_{max} of the Co-substituted samples was lower than that of the V-substituted sample, the zT_{max} was enhanced from 0.27 ($x = 0$) to 0.50 ($x = 0.04$) around 800 K due to the increase in the PF by Co substitution which leads to the decrease in γ and VEC.

CONCLUSIONS

We investigated the effects of Co substitution on the crystal structure, microstructure, and TE properties of melt-grown $MnSi_\gamma$. From obtained XRD patterns and EDS analysis, it was confirmed that MnSi precipitates were dissipated by Co substitution of 3–4%. The refined c-axis parameter, γ, dropped at $x = 0.02$, resulting in a smaller VEC for the Co-substituted sample compared with the Co-free sample. The electrical conductivity and Seebeck coefficient increased and decreased, respectively, by Co substitution, resulting from the increase in

carrier concentration. This result suggests that the carrier concentration can be controlled by the number of valence electrons of the elements and by the γ value. The lattice thermal conductivity of the Co-substituted sample greatly decreased compared with the Co-free sample. Consequently, zT was enhanced from ~ 0.3 for $x = 0$ to ~ 0.5 for $x = 0.04$ around 800 K.

ACKNOWLEDGMENTS

This work was supported by a Grant-in-Aid for JSPS Fellows (No. 18J11055). The authors thank T. Kawamata and T. Miyazaki of Tohoku University for their support in the Laue diffraction and EBSD measurement, respectively. We thank Iain Mackie, PhD, from Edanz Group (www.edanzediting.com/ac) for editing a draft of this manuscript.

CONFLICT OF INTEREST

The authors declare that they have no conflict of interest.

REFERENCES

1. Y. Kikuchi, T. Nakajo, K. Hayashi, and Y. Miyazaki, *J. Alloys Compd.* 616, 263 (2014).
2. Z. Du, T. Zhu, Y. Chen, J. He, H. Gao, G. Jiang, T.M. Tritt, and X. Zhao, *J. Mater. Chem.* 22, 6838 (2012).
3. T. Sakamoto, T. Iida, A. Matsumoto, Y. Honda, T. Nemoto, J. Sato, T. Nakajima, H. Taguchi, and Y. Takanashi, *J. Electron. Mater.* 39, 1708 (2010).
4. M. Kubouchi, K. Hayashi, and Y. Miyazaki, *Scr. Mater.* 123, 59 (2016).
5. A. Heinrich, H. Griessmann, G. Behr, K. Ivanenko, J. Schumann, and H. Vinzelberg, *Thin Solid Films* 381, 287 (2001).
6. J. Tani and H. Kido, *J. Appl. Phys.* 84, 1408 (1998).
7. S.W. Kim, M.K. Cho, Y. Mishima, and D.C. Choi, *Intermetallics* 11, 399 (2003).
8. U. Gottlieb, A. Sulpice, B. Lambert-Andron, and O. Laborde, *J. Alloys Compd.* 361, 13 (2003).
9. O. Schwomma, H. Nowotny, and A. Wittmann, *Monatsh. Chem.* 94, 681 (1963).
10. O. Schwomma, A. Preisinger, H. Nowotny, and A. Wittmann, *Monatsh. Chem.* 95, 1527 (1964).
11. H.W. Knott, M.H. Mueller, and L. Heaton, *Acta Crystallogr.* 23, 549 (1967).
12. G. Zwilling and H. Nowotny, *Monatsh. Chem.* 104, 668 (1973).
13. Y. Miyazaki, D. Igarashi, K. Hayashi, T. Kajitani, and K. Yubuta, *Phys. Rev. B* 78, 214104 (2008).
14. M.I. Fedorov and V.K. Zaitsev, *Thermoelectrics Handbook, Chap. 31*, ed. D.M. Rowe (Boca Raton: CRC Press, 2006), p. 3.
15. I. Aoyama, M.I. Fedorov, V.K. Zaitsev, F.Y. Solomkin, I.S. Eremin, A.Y. Samunin, M. Mukoujima, S. Sano, and T. Tsuji, *Jpn. J. Appl. Phys.* 44, 8562 (2005).
16. A.J. Zhou, T.J. Zhu, X.B. Zhao, S.H. Yang, T. Dasgupta, C. Stiewe, R. Hassdorf, and E. Mueller, *J. Electron. Mater.* 39, 2002 (2010).
17. Y. Miyazaki, Y. Saito, K. Hayashi, K. Yubuta, and T. Kajitani, *Adv. Sci. Tech.* 74, 22 (2010).
18. X. Chen, J. Zhou, J.B. Goodenough, and L. Shi, *J. Mater. Chem. C* 3, 10500 (2015).
19. A. Yamamoto, S. Ghodke, H. Miyazaki, M. Inukai, Y. Nishino, M. Matsunami, and T. Takeuchi, *Jpn. J. Appl. Phys.* 55, 020301 (2016).
20. Y. Miyazaki, H. Hamada, K. Hayashi, and K. Yubuta, *J. Electron. Mater.* 46, 2705 (2017).
21. Y. Miyazaki, H. Hamada, H. Nagai, and K. Hayashi, *Materials* 11, 926 (2018).
22. D.Y.N. Truong, H. Kleinke, and F. Gascoin, *Intermetallics* 66, 127 (2015).
23. X. Chen, L. Shi, J. Zhou, and J.B. Goodenough, *J. Alloys Compd.* 641, 30 (2015).
24. T. Kojima, I. Nishida, and T. Sakata, *J. Cryst. Growth* 47, 589 (1979).
25. V. Petricek, M. Dusek, and L. Palatinus, *Z. Kristallogr.* 229, 345 (2014).
26. J.C. Slater, *J. Chem. Phys.* 41, 3199 (1964).
27. The electrical conductivity of $(Mn_{0.95}Co_{0.05})Si_\gamma$ from Ref. [17] shown in Fig. 4(a) is 100 times higher than the original value in Ref. [17] because the unit of S/m in Fig. 3 in the reference appeared to be mistaken for S/cm.